Journal of
Marine Science and Engineering

MDPI

Article

Random Wave-Induced Momentary Liquefaction around Rubble Mound Breakwaters with Submerged Berms

Daniele Celli [1,*], Yuzhu Li [2], Muk Chen Ong [3] and Marcello Di Risio [1]

[1] Department of Civil, Construction-Architectural and Environmental Engineering (DICEAA)—Environamental and Maritime Hydraulic Laboratory (LIam) University of L'Aquila, 67100 L'Aquila, Italy; marcello.dirisio@univaq.it
[2] Department of Mechanical Engineering, Fluid Mechanics, Coastal and Maritime Engineering, Technical University of Denmark, 2800 Kongens Lyngby, Denmark; yuzhuli@mek.dtu.dk
[3] Department of Mechanical and Structural Engineering and Materials Science, University of Stavanger, 4036 Stavanger, Norway; muk.c.ong@uis.no
* Correspondence: daniele.celli@univaq.it

Received: 23 February 2020; Accepted: 1 May 2020; Published: 9 May 2020

Abstract: The effects of submerged berms in attenuating the momentary liquefaction beneath rubble mound breakwaters under regular waves were investigated in a recent study. The present work aims to investigate the momentary liquefaction probabilities around and beneath breakwaters with submerged berms under random waves. The interaction between waves and breakwaters with submerged berms has been simulated through a phase-resolving numerical model. The soil response to the seabed pressure induced by random waves has been investigated using a poro-elastic soil solver. For three different breakwater configurations, the liquefaction depths under random wave conditions have been compared with those cases under representative regular waves. In the present study, the offshore spectral wave height (H_{m0}) and the peak period (T_p) of irregular waves are used as representative regular wave parameters. Results reveal the importance of considering random waves for a safe estimation of the momentary liquefaction probability. Indication about the minimum number of random waves, which is required to properly catch the liquefaction occurrences, has been also addressed.

Keywords: berm; breakwaters; random waves; SWASH; momentary liquefaction; numerical models

1. Introduction

For the design of rubble mound breakwaters, it is important to analyze the structure response under environmental loads such as waves and currents (e.g., [1–4]), as well as storm surge events (e.g., [5,6]). Van Gent [7] and Celli et al. [8] argued that introducing a berm in the seaward side of rubble mound breakwaters can increase the stability of the rocks in the armor layer. Their research studies revealed that the presence of the berm enhances the wave energy dissipation before the waves reach the armor layer, leading to a reduced rock diameter required for the stability, compared with conventional rubble mound breakwaters.

Further to the structure response, when designing rubble mound breakwaters, the soil response and its effect on the foundation stability must be assessed. The stability of these structures can be threatened by geotechnical causes, such as the wave-induced soil liquefaction in the vicinity of the structure. The excess pore pressure induced by the wave propagation is accountable for the triggering of the residual and the momentary liquefaction (e.g., [9–11]). The residual liquefaction, typical of loose sand deposits, occurs when the wave-induced excess of pore water pressure overcomes the overburden

pressure, making the soil particles completely unbound [12]. The momentary liquefaction generally occurs in dense sands if the upward pore pressure gradient, induced by wave troughs, overcomes the initial vertical effective stress (e.g., [13]).

Besides increasing the armor layer stability, Celli et al. [13] showed that deploying a submerged berm is valuable in reducing wave-induced momentary liquefaction, compared with a straight sloped conventional rubble mound breakwater. In particular, a parametric study was carried out by varying the berm geometry in terms of its height and its length, keeping constant the armor layer and the berm porosity, the elastic soil properties, the offshore regular wave conditions, and the water depth. The parametric study among different berm schemes has identified the best berm geometric configuration in attenuating momentary liquefaction occurrences. The parametric study performed by Celli et al. [13] is based on regular wave assumption, despite random waves always appearing in the real ocean environments.

To date, a few research studies considered the effect of random waves on the soil responses and liquefaction processes. Sumer et al. [14] investigated the effects of random waves on the displacement of a pipe buried in soil subjected to residual liquefaction. The comparison with regular wave results revealed that the best agreement, concerning the number of waves causing liquefaction, occurred in correspondence of $H = H_s/\sqrt{2} \simeq 0.7H_s = H_{rms}$ (if the Rayleigh distribution of wave heights applies) and $T = T_z$. Here, H and T are the wave height and wave period of regular waves, respectively. H_s and T_z are the significant wave height and the mean zero up-crossing period of random waves, respectively. H_{rms} is the root-mean-square wave height of the random sea state. Therefore, the best agreement turned out for two different wave trains (i.e., regular and random) characterized by the same energy. Liu and Jeng [15] developed a semi-analytical solution for the soil response induced by random waves and seabed liquefaction. In particular, the influence of random waves on the soil response was investigated and compared with the corresponding representative regular waves (i.e., $H = H_s/\sqrt{2}$ and $T = T_z$) results. They also carried out a parametric study investigating the effects of the wave height and period, the seabed thickness, the degree of saturation, and the soil permeability on the soil response. Xu and Dong [16] carried out a numerical study about the liquefaction occurrences due to random waves, by identifying the liquefaction depths through probability distributions. Their results indicate that the liquefaction depth induced by random waves is larger than the one induced by regular waves. The latter was determined by adopting an ensemble approach, calculating the liquefaction depths caused by all possible regular wave heights following the Rayleigh distribution and then determining a representative liquefaction depth. Zhao et al. [17] developed a poro-elastoplastic numerical model to analyze the random wave-induced liquefaction behaviors of loosely deposited seabed foundations, taking into account both residual and oscillatory soil responses. Their results revealed that the use of monochromatic wave conditions leads to the underestimation of the liquefaction phenomenon.

The aforementioned studies, although underlining how important the use of random wave conditions are in assessing the maximum liquefaction depth and their implications in the design process, did not include the presence of any structure on the soil in their works. In the present study, the momentary liquefaction probability induced by random waves has been investigated in the presence of rubble mound breakwaters with submerged berms. In order to analyze the effects of random waves on the momentary liquefaction phenomena, a comparison with the results concerning the corresponding representative regular wave loading, provided by Celli et al. [13], has been carried out. In particular, three geometric configurations have been selected (see Figure 1): a straight sloped conventional rubble mound breakwater without a berm and two rubble mound breakwaters with submerged berms marked by $h_b/h_t = 0.590$, $L_b/L_w = 0.356$, and $h_b/h_t = 0.190$, $L_b/L_w = 0.356$, respectively (being h_t the water depth at the toe of the berm, h_b the water depth over the berm, L_b the berm length, and L_w the wave length at the berm toe). The first one has been considered as the reference configuration. This allows for evaluating if the introduction of a submerged berm (i.e., second and third configurations) leads to a reduction of the momentary liquefaction probability under random waves as for regular waves. The second configuration represents the optimal design choice to limit

liquefaction phenomena under regular wave conditions, as discussed in Celli et al. [13]. The third configuration has been selected to further evaluate the liquefaction probability under random waves with a different berm configuration.

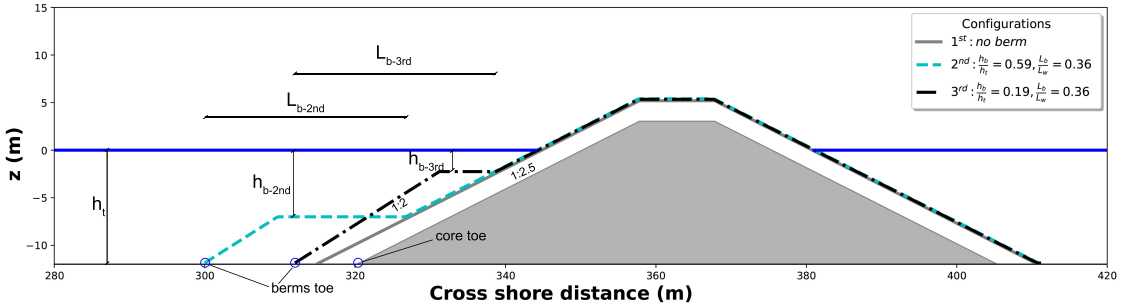

Figure 1. Tested geometric configurations: a rubble mound breakwater without a berm and two rubble mound breakwaters with submerged berms characterized by $h_b/h_t = 0.590$, $L_b/L_w = 0.356$, and $h_b/h_t = 0.190$, $L_b/L_w = 0.356$, respectively.

It is worth mentioning that several experimental (e.g., [18]) and numerical (e.g., [19]) studies revealed no occurrences of momentary liquefaction beneath the breakwater since the overburdened pressure is considerably increased by the structure weight. As for Celli et al. [13], in the work presented herein, all the wave-induced momentary liquefaction occurrences beneath the breakwaters are due to the discontinuous contact between the soil and the berm rocks, aimed to outline the absence of a transition layer (i.e., bedding layer) under the berm. Then, the results of the present study is useful for the scenario in which the load of the berm rocks is transmitted to the soil only through the contact area (i.e., no transition layer under the berm, see Figure 2). It can also provide a safe estimation of the transition layer thickness under the berm, if it is taken into account during the design phase.

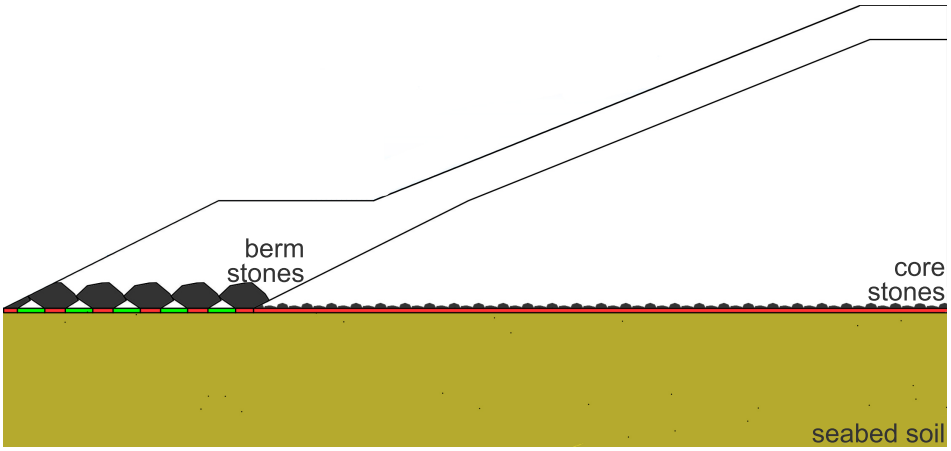

Figure 2. Sketch of assumed load distribution under a porous structure: red zones refer to contact areas, where the load is transferred to the soil. Green zones refer to unloaded areas.

The features of the present work can be summarized as follows. For different configurations of rubble mound breakwaters with submerged berm, the dynamic seabed pressure induced by random waves has been computed via the open-source numerical model SWASH [20]. On the other hand, the seabed consolidation state and the response under dynamic wave loading have been evaluated through a poro-elastic soil model discussed in Li et al. [21] within the OpenFOAM® framework. A coupling boundary condition (one-way) has been adopted to simulate the interaction between multiple physical phases, including water waves, structure and the seabed. Then, the liquefaction depths induced by random waves have been evaluated and compared with those derived from the regular wave test cases provided by Celli et al. [13]. The number of random waves

required to properly describe the momentary liquefaction occurrences and their magnitude has been investigated as well.

2. Numerical Approach

2.1. Numerical Models and Coupling Algorithm

SWASH has been used to evaluate the dynamic seabed pressure induced by random waves, within the wave-structure interaction framework. It is a phase resolving numerical model solving the shallow water equations including:

- a non-hydrostatic pressure term (derivable from the incompressible Navier–Stokes equations);
- a module for porous flow based on the Forchheimer's formulations.

Hence, two extra dissipative terms, f_l (laminar) and f_t (turbulent) are considered in the porous momentum equations. In particular:

$$f_l = \alpha_0 \frac{(1-n)^3}{n^2} \frac{\nu}{D_{n50}^2} \qquad f_t = \beta_0 \frac{(1-n)}{n^3} \frac{1}{D_{n50}} \tag{1}$$

where α_0 and β_0 are the Forchheimer's coefficients, n is the porosity, and D_{n50} represents the nominal diameter.

About the governing equations, the layer-integrated continuity equations reads as follows [20]:

$$\frac{\partial h_k u_k}{\partial x} - u \frac{\partial z}{\partial x}\Big|_{z_{k-1/2}}^{z_{k+1/2}} + w_{k+1/2} - w_{k-1/2} = 0 \tag{2}$$

where x is the horizontal coordinate, h_k is the thickness of the layer k, z is the elevation of the interface between two layers (being $z_{k-1/2}$ the interface between the layer $k-1$ and the layer k and $z_{k+1/2}$ the interface between the layer k and the layer $k+1$), u is the layer-integrated horizontal velocity, and $w_{k\pm1/2}$ is the vertical velocity at the interfaces between two layers.

The layer-integrated horizontal momentum equation reads as follows:

$$\begin{aligned} &\frac{\partial h_k u_k}{\partial t} + \frac{\partial h_k u_k^2}{\partial x} + \bar{u}^z_{k+1/2}\omega_{k+1/2} - \bar{u}^z_{k-1/2}\omega_{k-1/2} + \\ &+ g h_k \frac{\partial \zeta}{\partial x} + \frac{\partial h_k \bar{q}^z_k}{\partial x} - q_{k+1/2}\frac{\partial z_{k+1/2}}{\partial x} + q_{k-1/2}\frac{\partial z_{k-1/2}}{\partial x} = 0 \end{aligned} \tag{3}$$

where t is the elapsed time, $\bar{u}^z_{k\pm1/2}$ is the horizontal velocity estimated at the layer interfaces $z_{k\pm1/2}$, $\omega_{k\pm1/2}$ is the vertical velocity relative to layer interface $z_{k\pm1/2}$ (defined as the difference between the vertical velocity along the streamline and the vertical velocity along the interface), g is the gravitational acceleration, ζ is the free surface elevation, $q_{k\pm1/2}$ is the non-hydrostatic pressure defined at the layer interfaces, and $\bar{q}^z_k$ is the arithmetic mean of the non-hydrostatic pressure at the layer interfaces $z_{k\pm1/2}$.

The layer-integrated vertical momentum equation reads as follows:

$$\frac{\partial h_{k+1/2} w_{k+1/2}}{\partial t} + \frac{\partial h_{k+1/2} \bar{u}^z_{k+1/2} w_{k+1/2}}{\partial x} + \bar{w}^z_{k+1}\bar{\omega}^z_{k+1} - \bar{w}^z_k \bar{\omega}^z_k + 2\bar{q}^z_k = 0 \tag{4}$$

where $h_{k+1/2}$ is the arithmetic mean of the layer thicknesses h_k and h_{k+1}, $\bar{w}^z_{k(+1)}$ is the arithmetic mean of the vertical velocities at the layer interfaces $z_{k(+1)\pm1/2}$, and $\bar{\omega}^z_{k(+1)}$ is the arithmetic mean of the vertical velocities relative to the layer interface at the layer interfaces $z_{k(+1)\pm1/2}$.

The details concerning the numerical procedures and the boundary conditions are shown in [22–24].

With reference to the soil model, it has been assumed that:

(i) the seabed has constant thickness;

(ii) the soil has a degree of saturation $S_r = 0.975$;
(iii) the soil skeleton is characterized by elastic properties, obeying to Hooke's law;
(iv) the Young's modulus, the soil permeability, and the Poisson's ratio vary in horizontal and vertical directions (i.e., anisotropic condition).

The soil model, developed within the OpenFOAM® framework (e.g., [21]), solves the classical Biot's consolidation equations [25], simulating the interaction between the pore fluid and the solid skeleton. The behavior of the porous medium under random wave loading is governed by the quasi-static momentum balance equation for soil mixture and the mass balance equation of the pore fluid based on Darcy's law.

Quasi static-momentum balance equation reads as follows:

$$\nabla \cdot \left[\mathbf{C} : \frac{1}{2} \left(\nabla \mathbf{U} + (\nabla \mathbf{U})^T \right) \right] - \nabla p = 0 \tag{5}$$

where $\mathbf{U}$ is the soil (skeleton) displacement, p is the pore fluid pressure, and $\mathbf{C}$ is the elastic stiffness tensor. For anisotropic soil materials, the two-dimensional orthotropic elastic stress-strain relation can be expressed in a 3×3 matrix notation:

$$\boldsymbol{\sigma}' = \begin{pmatrix} \sigma'_{xx} \\ \sigma'_{zz} \\ \sigma_{xz} \end{pmatrix} = \begin{bmatrix} A_{11} & A_{12} & 0 \\ A_{12} & A_{22} & 0 \\ 0 & 0 & A_{33} \end{bmatrix} \begin{pmatrix} \epsilon_{xx} \\ \epsilon_{zz} \\ \epsilon_{xz} \end{pmatrix} = \mathbf{C} : \epsilon \tag{6}$$

where $\boldsymbol{\sigma}'$ is the effective stress tensor and $\epsilon = \frac{1}{2} \left[\nabla \boldsymbol{U} + (\nabla \boldsymbol{U})^T \right]$ is the stress tensor. The four independent coefficients A_{ij} can be calculated from Young's modulus E_i, Poisson's ratio ν_{ij}, and the shear modulus G_{ij} (e.g., [13]).

The mass balance equation of the pore fluid reads as follows:

$$\frac{n}{K'} \frac{\partial p}{\partial t} = -\frac{1}{\gamma_w} \nabla \cdot (\mathbf{k} \cdot \nabla p) + \frac{\partial}{\partial t} (\nabla \cdot \mathbf{U}) \tag{7}$$

where n denotes the soil porosity, γ_w represents the specific weight of the water in the soil, and $\mathbf{k}$ denotes the diagonal permeability tensor with values k_x and k_z. These equations are detailed in Celli et al. [13], based on the work of Li et al. [21].

The coupling between the two numerical tools, i.e., SWASH and OpenFOAM®, has been achieved by data mapping at the shared boundaries (see Figure 3). A similar approach was adopted in the works of Ye et al. [19], Li et al. [21,26], and Celli et al. [13]. First, the interaction between waves and the porous structure is simulated. Then, the pressure p_d induced by random waves, acting on the seabed and beneath the porous structure, is provided to the soil domain via the wave–seabed interface and structure–seabed interface (see Figure 3) as a dynamic boundary condition. The poro-elastic soil displacements are assumed to be small enough to not affect the wave-porous structure domain.

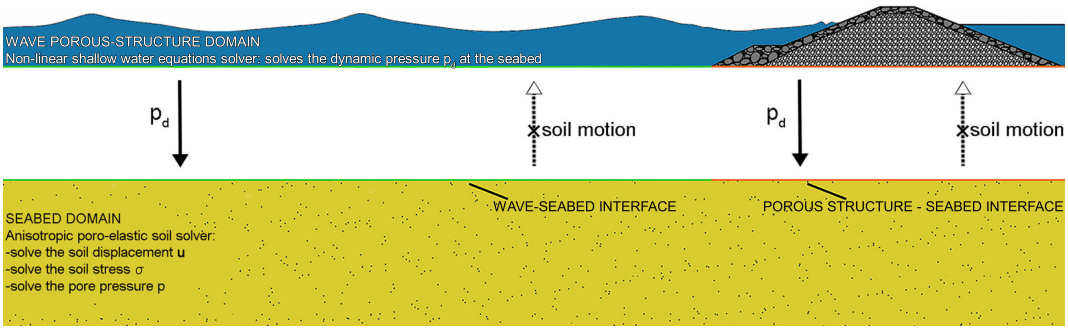

Figure 3. One-way boundary condition for wave-structure-seabed interaction.

2.2. Models Validation

The SWASH model was already used in previous studies (e.g., [27–32]). The model reliability in detecting the interaction between rubble mound breakwater with submerged berms and the incident random waves was validated by Celli et al. [8]. A power spectra comparison between computed and observed data was carried out (see their Figure 4), showing satisfactory agreement. The poro-elastic soil model, implemented in OpenFOAM®, was validated by Li et al. [21], on the basis of experimental data from Tsai and Lee [33] (e.g., see their Figures 2–4). To further verify the poro-elastic soil model for the present problems, in which porous structures are involved, a comparison with experimental data has been carried out. Since experimental data of pore pressure induced by irregular wave trains under rubble mound breakwaters are lacking, the validation resorts to the work of Bierawski and Maeno [34], concerning only regular waves. In particular, a laboratory small-scale experiment was performed to study the wave-induced pore pressure over a submerged breakwater and in the sandy bed beneath the structure. The experimental layout is shown in the upper panel of Figure 4. The sandy bed was 3 m long, and 0.40 m thick. The grain size d_{50} was 0.25 mm, the density ρ_s = 2650 Kg/m^3, the porosity n $\simeq$ 0.4 and the permeability coefficient k = 1.2×10^{-4} m/s. The breakwater had steep slopes 1:2. The structure crest was 0.30 m high and 0.30 m long. It was made by stones with a mean diameter d_{50} = 15 mm. The porosity coefficient was n $\simeq$ 0.35.

On the basis of the one-way coupling algorithm, the wave-porous structure domain has been simulated in SWASH by adopting a constant horizontal spacing dx = 0.01 m. The submerged breakwater has been simulated adopting a porous layer inside the computational domain. A volumetric porosity value of 0.4 has been used. A still water level has been applied as initial condition (h = 0.30 m).

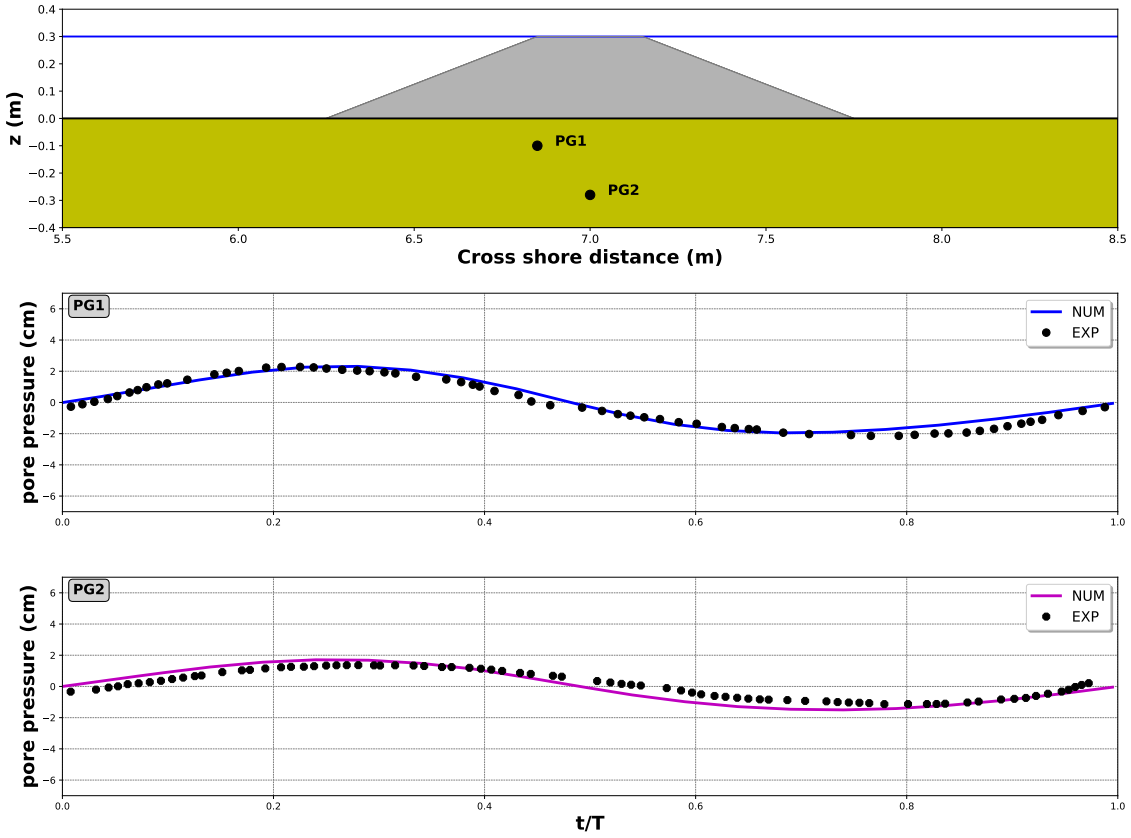

Figure 4. Upper panel: experimental layout adopted by Bierawski and Maeno [34]. Middle and lower panels: comparison between experimental and numerical results in terms of pore pressure, collected at PG1 and PG2, respectively.

In the soil model, the computational domain has been discretized by adopting an orthogonal mesh characterized by a cell resolution equal to 0.01 m along the x-direction and 0.01 m along the z-direction (3×10^3 elements). The computational domain has been extended up to 1 m downward to avoid the effect of the bottom boundary. The seabed sand properties are based on the experimental measurement carried out by Bierawski and Maeno [34]. Under the action of regular waves, characterized by H = 0.06 m and T = 2 s, the observed pore pressures at PG1 (x = 6.85 m z = −0.1 m) and PG2 (x = 7.0 m z = −0.28 m) have been compared with the computed one. The good agreement between the numerical and the experimental results, depicted in the middle and lower panels of Figure 4, confirms the reliability of the present model to catch the wave-induced pore pressure spatio-temporal variation.

3. Numerical Investigations

According to Celli et al. [13], the SWASH computational grid spatial resolution has been adopted to accomplish reliable numerical accuracy. For each simulation, the total length of the computational wave domain is equal to 411 m. In the horizontal direction, the cell size is set at 0.2 m. To properly describe the wave frequency dispersion, the computational domain has been divided into three vertical terrain-following layers. The layer thickness, which is the distance between two consecutive layer interfaces, has been defined in an absolute way, by adopting a fixed layer thickness. The sum of the layer thicknesses locally equals the water depth. A water level time series generating random waves is imposed at the offshore side, considered as weakly reflective boundary. For each test, about 625 waves have been simulated (i.e., $T_r = 5000\ s$, T_r being the duration of the simulations). At the onshore side, the Sommerfeld radiation condition (e.g., [20]) is imposed. The seabed response to the wave-induced seabed pressures has been investigated through an anisotropic poro-elastic soil solver [21], developed within the OpenFOAM® framework. A grid convergence study was carried out by Celli et al. [13], and consequently, 2.7×10^5 grid points have been used to evaluate the soil response within the study described herein. The seabed domain is 450 m long and 30 m thick. To avoid the effect of the onshore boundary, the domain has been extended of 39 m from the breakwater end. For comparative purporses, the soil porosity n is set to 0.3 and the saturation factor S_r is set to 0.975. It should be stressed that a reduction of S_r may lead to an increased soil portion affected by momentary liquefaction (e.g., [12,35]). The anisotropic soil properties are shown in Table 1. The adopted values for soil permeability (i.e., k_x = 0.005 m/s and k_z = 0.001 m/s) are typical of medium/coarse sand, to which this study refers. Within the seabed domain, the adopted boundary conditions read as follows:

(1) at the structure–seabed and wave–seabed interfaces, the traction in the soil is zero. The effective soil stresses vanish. Therefore, the pore pressure equals the dynamic pressure acting on the aforementioned interfaces;
(2) at the lateral boundaries and at the bottom of the seabed, the normal pore pressure gradient is zero, the soil skeleton being allowed to slip.

The soil responses and liquefaction depths in the vicinity of a breakwater with submerged berms in regular waves were obtained by Celli et al. [13], considering waves characterized by $H = 4$ m and $T = 8$ s. In order to compare the soil responses induced by regular and random waves, equivalent wave parameters (i.e., wave period and wave height) between the regular and random wave conditions should be chosen.

Table 1. Soil parameters for wave–structure–seabed interaction (e.g., [13]).

Seabed Parameters (Directional Values)		
Young's modulus (N/m^2)	$E_x = 1.2 \times 10^7$	$E_z = 2.0 \times 10^7$
Poisson's ratios	$\nu_{zx} = 0.40$	
Shear modulus (N/m^2)	$G_{zx} = 5 \times 10^6$	
Permeability (m/s)	$k_x = 0.005$	$k_z = 0.001$

In the present study, similar to Liu and Jeng [36] (which considered $H_s = H, T_s = T$), the offshore spectral wave height (H_{m0}) and the peak period (T_p) of irregular waves are used as representative regular wave parameters: $H_{m0} = H = 4$ m (being $H_{m0} = 4\sqrt{m0}$; $H_{m0} = H_s$ if deep water conditions apply); $T_p = T = 8$ s. According to Rayleigh distribution, $H_{m0} = H_s \simeq 1.6\bar{H}$, $T_s \simeq 1.2\bar{T} \simeq 0.93T_p$ (for JONSWAP-type spectra with a peak enhancement factor $\gamma = 3.3$), where $\bar{H}$ and $\bar{T}$ are the mean wave height and the mean wave period of random waves, respectively (e.g., [37]). Then, in comparison with Liu and Jeng [36], the representative regular waves selected in the present study share the wave height definition (i.e., $H_{m0} = H_s$). On the other hand, a longer wave period is considered ($T_p \simeq 1.07\ T_s$).

The time-series of surface elevation, derived synthesizing a JONSWAP spectrum with $\gamma = 3.3$, is illustrated in Figure 5.

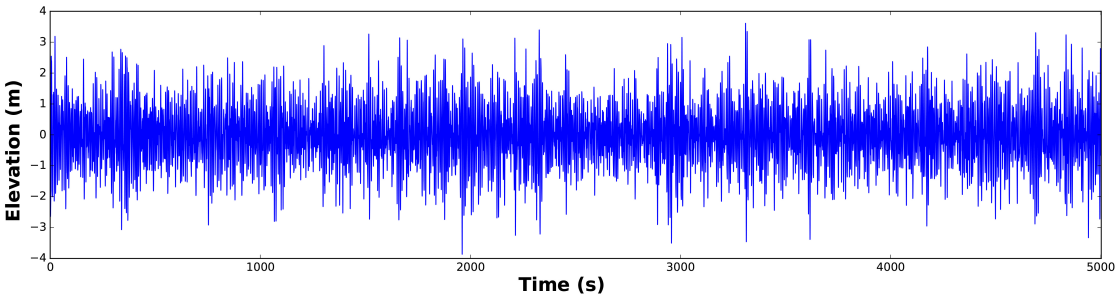

Figure 5. Time history of the simulated random waves, equal for each simulation. The represented water levels do not take into account the onshore water depth h = 12 m.

4. Results and Discussion

As an example, in Figure 6, the wave-induced transient pore pressure is depicted along with the seepage flow at t = 1281.6 s, for the rubble mound breakwater without a submerged berm (i.e., first configuration).

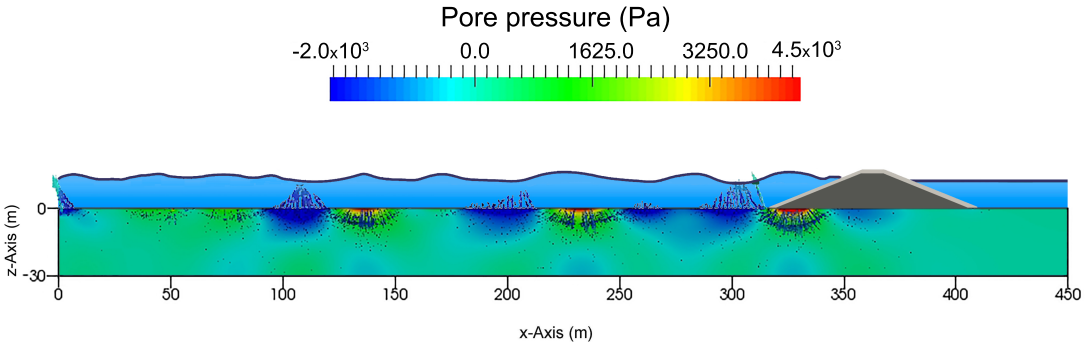

Figure 6. Wave-induced seabed response concerning a breakwater without submerged berm: transient pore pressure along with the seepage flow at t = 1281.6 s ($H_{mo} = 4$ m, $T_p = 8$ s).

For the depicted random wave train, the magnitude of dynamic seabed pressure relies on the amplitude of the single wave crest and trough. As expected, wave crests cause positive transient pore pressure, whilst the transient pore pressure becomes negative under wave troughs. In the same vein, the direction of the seepage flow is related to the wave phases (e.g., [38]). When the upward pore pressure gradient exceeds the vertical initial effective stress, the momentary soil liquefaction will take place, potentially affecting the structure stability. When the seepage force is oriented downward, the seabed does not liquefy since it causes a higher contact effective stresses in the soil [38].

In order to take into account the stress increase in the seabed due to the structure gravitational load, the liquefaction criterion adopted by Zen and Yamazaki [9], expressed by:

$$p(z,t) - p(0,t) \geq -(\gamma_s - \gamma_w)z \quad (8)$$

has been modified as follows:

$$p(z,t) - p(0,t) \geq \sigma'_z \tag{9}$$

where σ'_z is the initial vertical effective stress related to the gravitational forces from the consolidation phase. The criterion was already used in the works of Zhao et al. [17], Sui et al. [39], Li et al. [21], and Celli et al. [13]. The wave-induced soil liquefaction occurrences are strongly influenced by the consolidation status, which is experienced by the soil after the breakwater construction, under the hydrostatic water pressure and the structure weight. Therefore, the vertical effective stresses σ'_z equilibrium distribution reached by the seabed foundation after the consolidation process has been pre-assessed and then used as the initial condition for the momentary liquefaction analysis.

Figure 7 shows the distribution in the soil of the initial vertical effective stresses σ'_z, at the end of the consolidation phase for the simulated test case with $h_b/h_t = 0.19$ and $L_b/L_w = 0.35$. A negative value of σ'_z represents the compression of the soil skeleton. The higher (absolute) values of σ'_z appear under the breakwater. In addition, Figure 7 reveals a compressive (i.e., negative) stress concentration in two zones: at the core–berm interface and at the end of the breakwater. This is due to the different distributions of gravitational load between the core and the submerged berm and also between the loaded and unloaded zones at the end of the structure.

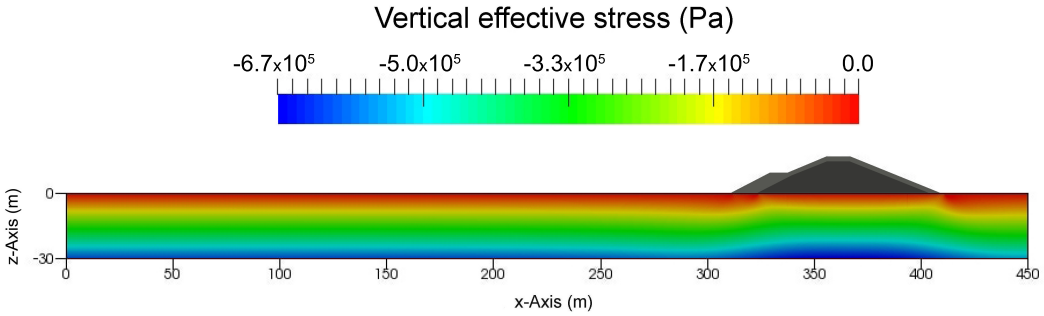

Figure 7. Vertical effective stress σ'_z at the end of the consolidation process concerning a breakwater with submerged berm with $h_b/h_t = 0.19$ and $L_b/L_w = 0.35$.

After the assessment of the initial vertical effective stress distributions for the three configurations depicted in Figure 1, the criterion outlined by Equation (9) has been applied for both random and regular wave loads.

Figure 8 (upper panel) shows the maximum liquefaction depths for a straight sloped rubble mound breakwater without a berm, under the actions of regular and random waves, respectively.

The middle and the lower panels show the maximum liquefied depths induced by regular and random waves, respectively. In particular, the areas have been split into two zones: the internal subareas (i.e., cyan zones) show the maximum liquefaction depths beneath the structure, whilst the external ones (i.e., blue zones) show the maximum liquefaction depths ahead of the structure, down to the breakwater toe. In each subarea, the maximum local depth has been evaluated along with the mean local depth (i.e., resulting from the subarea value divided by its superficial length). From the inspection of the middle and the lower panels, it turns out that the maximum internal liquefaction subarea induced by random waves is about 21% greater than the one induced by regular waves. The maximum internal liquefaction depth (henceforth referred to as d_{max_int}) is equal to 2 m for the random wave loads, about 14% greater than the regular wave case. In front of the structure, the maximum external liquefaction depth (henceforth referred to as d_{max_ext}) reaches about 1 m if random wave loads are considered, equivalent to a reduction of about 30% compared to the regular wave case. For both wave load types, the internal mean maximum value (hereinafter referred to as $\bar{d}_{int}$) is greater than the external one (i.e., $\bar{d}_{ext}$), confirming that for a rubble mound breakwater without a berm, the most prone zone to the momentary liquefaction is the area below the armor layer. The liquefaction is even more severe under the armor layer if random wave loads are considered (i.e., $\bar{d}_{int} \gg \bar{d}_{ext}$). It could be

hence particularly useful to evaluate if also under random wave actions, the presence of submerged berms tends to attenuate momentary liquefaction occurrences. In this regard, Figure 9 presents the maximum liquefaction depths concerning a rubble mound breakwaters with two submerged berm configurations, characterized by $h_b/h_t = 0.59$, $L_b/L_w = 0.36$ (right panels) and $h_b/h_t = 0.19$, $L_b/L_w = 0.36$ (left panels), respectively, under the action of regular (middle panels) and random (lower panels) waves. The fluctuating momentary liquefaction trend under the berm, particularly evident in the middle right panel of Figure 9 is due to the discontinuous contact between the soil and the berm rocks. Due to the rock arrangement, loaded zones (i.e., below the rocks) and unloaded zones (i.e., areas between two closely rocks) occur, as shown in Figure 2. In the contact area, the weight of the rocks increases the vertical effective stresses, decreasing the liquefaction probability. On the contrary, the existence of unloaded zones leads to a greater possibility of soil liquefaction in comparison with the loaded areas.

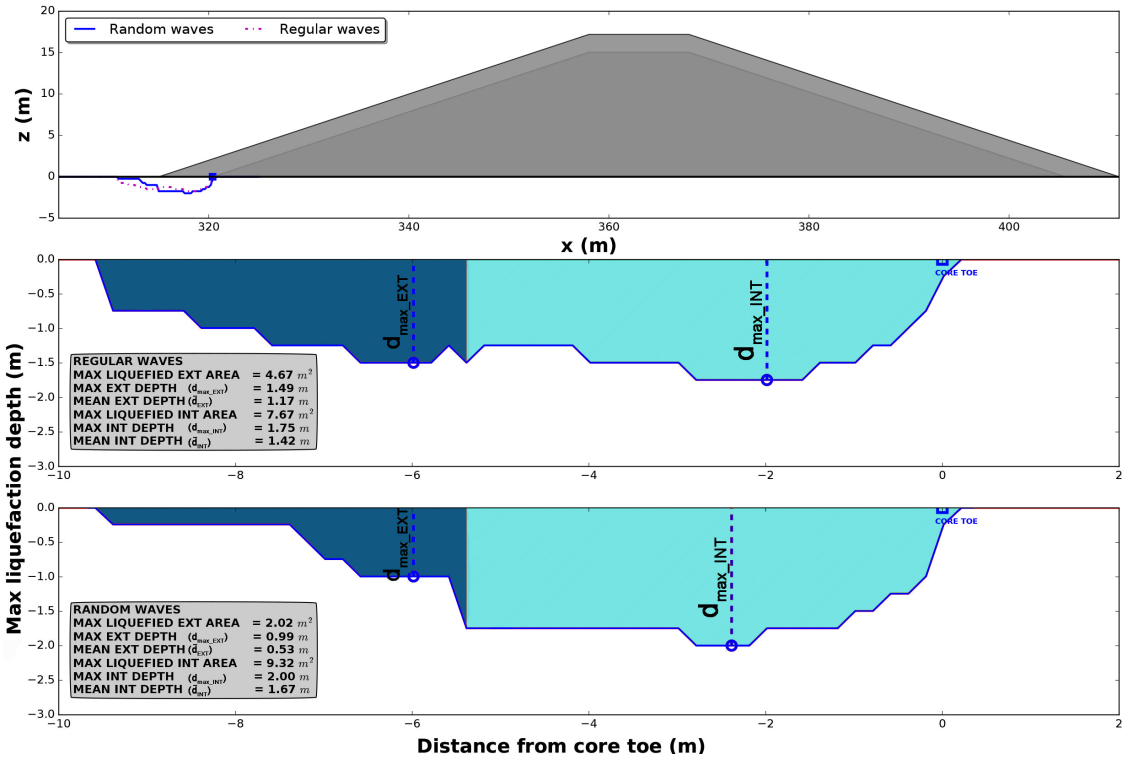

Figure 8. Wave-induced momentary liquefaction concerning a straight sloped conventional rubble mound breakwater without a berm. Upper panel: maximum depth of momentary liquefaction induced by regular and random waves around and beneath the structure. Middle panel: zoom of the maximum liquefied area induced by regular waves splits into two zones, in accordance with the location of the liquefaction occurrences. Blue subareas refer to maximum liquefaction depth ahead of the structure, down to the breakwater toe. Cyan subarea refers to maximum liquefaction depth below the structure. Lower panel: zoom of the momentary liquefaction maximum area induced by random waves.

From the comparison between the lower panels of Figures 8 and 9, it clearly appears how the submerged berms deployment reduces the momentary liquefaction depth, even if random waves are considered. Indeed, the lower berm characterized by $h_b/h_t = 0.59$ (right panel) shows a drop of d_{max_int} down to 1.49 m, corresponding to a decrease of about 25% in comparison to a straight sloped conventional breakwater. It should be noted that the maximum liquefied area for the conventional rubble mound breakwater of Figure 8 is lower than the liquefied areas of Figure 9 concerning rubble mound breakwaters with submerged berm. This is because the contact length between the

seabed and the structure increases as the berm grows in length. However, as already outlined in Celli et al. [13], this does not mean an increase of potential structure failure of the breakwater core.

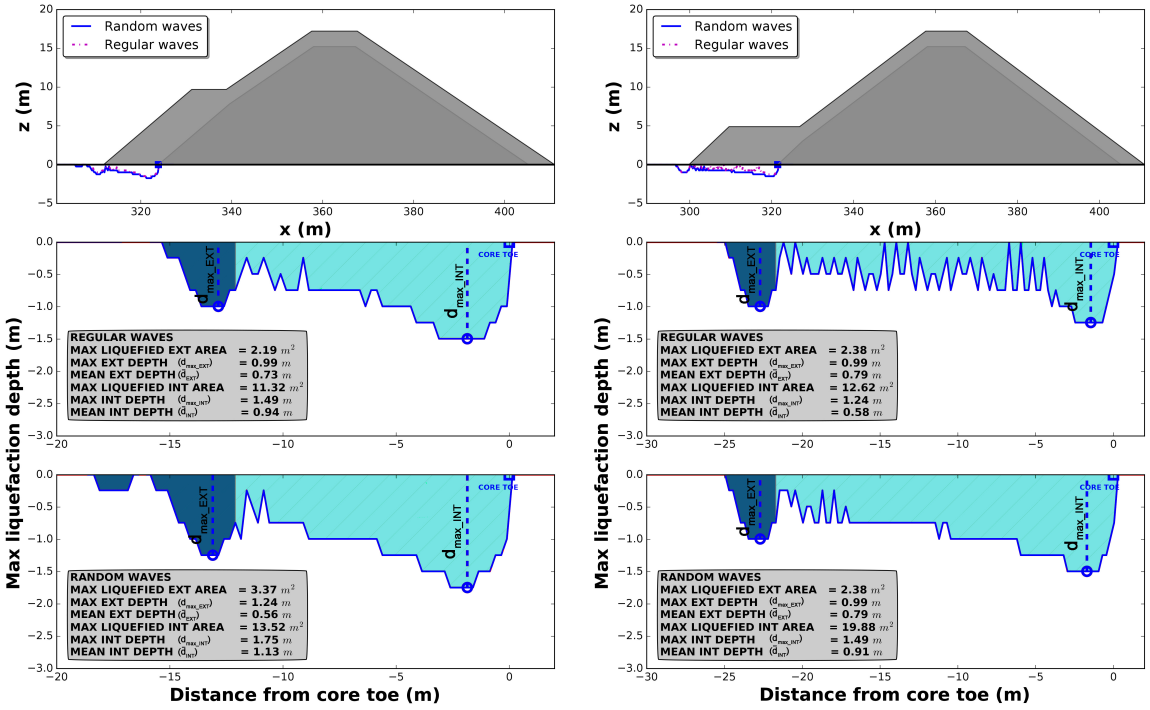

Figure 9. Wave-induced momentary liquefaction concerning breakwaters with submerged berms marked by h_b/h_t = 0.19 and L_b/L_w = 0.36 (**left** panels), h_b/h_w = 0.59 and L_b/L_w = 0.36 (**right** panels). Upper panels: maximum depth of momentary liquefaction around and below the structure. Middle panels: zoom of the maximum liquefied area induced by regular waves splits into two zones, in accordance with the location of the liquefaction occurrences. Blue subareas refer to maximum liquefaction depth ahead of the structure, down to the breakwater toe. Cyan subareas refer to maximum liquefaction depth below the structure. Lower panels: zoom of the momentary liquefaction maximum area induced by random waves.

Looking again at the lower panels of Figure 9, differences of d_{max_int} between the two configurations characterized by the same ratio of L_b/L_w and different values of h_b/h_t are observed. In particular, for the lower berm (right panels), d_{max_int} is reduced about 15%. Therefore, as already found in Celli et al. [13] for the regular wave case, even under random wave loading, the berm characterized by $h_b/h_t = 0.59$ reveals the capability in reducing the momentary liquefaction occurrences. This attributes to the right compromise between the initial vertical effective stress reduction and the seabed pore pressure attenuation, typically for this kind of berm configuration.

Focusing on the comparison among middle and lower panels of Figure 9, it shows how, under random wave loading, the effect of random waves (lower panels) modify the liquefied areas as compared to that under regular waves. The liquefaction depths can be regarded as a stochastic variable. Hence, numerical results can be further examined by using the Empirical Cumulative Distribution Function (i.e., ECDF). In order to investigate the effects of random waves on momentary liquefaction as compared to the regular waves, the ECDF of the percentiles of liquefaction depths has been evaluated for both the berm configurations. Figure 10 (upper panels) shows the percentiles of momentary liquefaction depths d_i (where i represents the percentile) induced by regular waves, for the two rubble mound breakwaters with submerged berms characterized by $h_b/h_t = 0.19$, $L_b/L_w = 0.35$ (left panels) and $h_b/h_t = 0.59$, $L_b/L_w = 0.35$ (right panels), respectively.

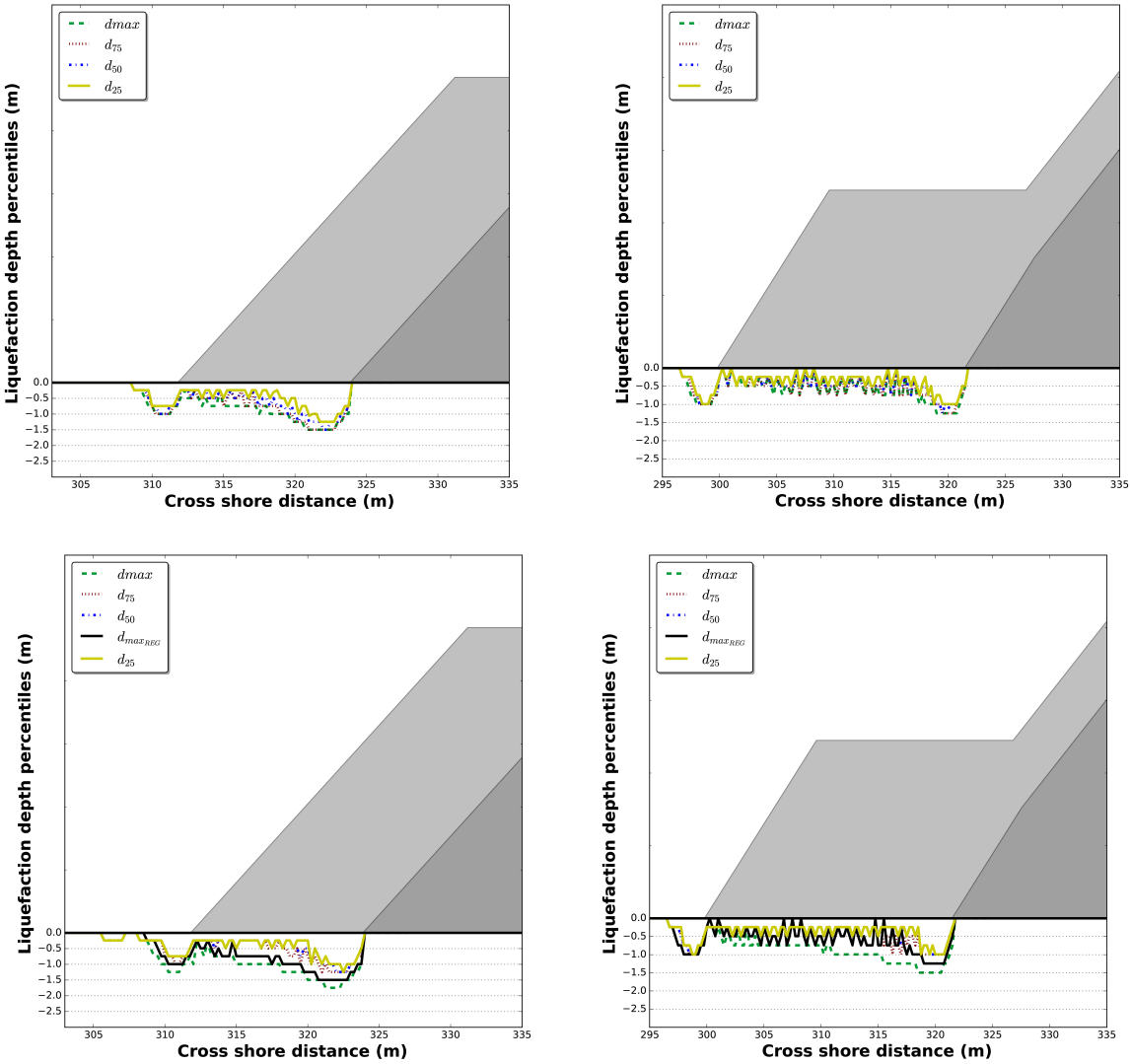

Figure 10. Momentary liquefaction depth percentiles induced by regular and random waves. Left panels refer to submerged berms characterized by $h_b/h_t = 0.19$, $L_b/L_w = 0.35$. Right panels refer to submerged berms characterized by $h_b/h_t = 0.59$, $L_b/L_w = 0.35$. Upper panels refer to momentary liquefaction induced by regular waves. Lower panels refer to momentary liquefaction induced by random waves.

Regardless of the selected configurations, it appears that the momentary liquefaction depths induced by regular waves are almost the same values for different considered percentiles. This is not surprising since the wave regularity entails that, in each point of the seabed, momentary liquefaction depths vary periodically, achieving almost the same maximum values over the time. The lower panels of Figure 10 present the percentiles of the momentary liquefaction depths induced by random waves, as well as the maximum momentary liquefaction depths induced by regular waves, for the two different berm configurations. In Figure 10, it appears that a similar trend of liquefaction depth along the x-axis under random waves to that under regular waves is obtained. However, the maximum momentary liquefaction depths induced by random waves are larger than the ones induced by regular waves, i.e., d_{max} due to irregular waves are greater than d_{maxREG} due to regular waves. Therefore, using representative regular wave parameters, i.e., $H = H_{m0}$, $T = T_p$ to assess the momentary liquefaction probability will lead to an underestimation of the liquefaction depth in the real ocean conditions. Although using the representative regular wave condition can reduce a large

amount of computational time, a safer design should hence be based on the estimation of momentary liquefaction induced by random waves.

In order to properly describe the momentary liquefaction occurrences and their magnitude induced by random waves, it is important to know the optimal number of random waves that should be simulated. In this study, for each configuration, about 625 waves have been reproduced according to the water level time-history depicted in Figure 5. To evaluate if the reproduced number of waves suffices or would have been reduced, the values of the maximum liquefaction depths as a function of the simulated number of waves have been calculated for each tested configuration. The liquefaction depths have been detected where they assume the maximum data value, i.e., at x $\simeq$ 322 m for both the configurations, as illustrated in upper panels of Figure 9. Within time series of liquefaction depth, temporal windows of different duration (i.e., 200 s, 500 s, 1000 s, 1500 s, 2000 s, 3000 s, 4000 s, 5000 s) have been identified. By moving each time window over the single time series, a dataset of maximum liquefaction depth has been calculated for each window duration, i.e., for a specific number of individual waves (e.g., 200 s are equal to about 25 individual waves). From each dataset, the mean values and the standard deviations of maximum liquefaction depth have then been evaluated. The results are shown in Figure 11, where in the blue boxes the percent differences with respect to the maximum liquefaction depth achieved for 625 waves (square markers) are indicated. Through the use of gray vertical bars, the standard deviation is also depicted. From both the panels, Figure 11 shows how the convergence has been reached for each configuration. Moreover, it is evident that it is important to consider a sufficient number of waves. For example, in the lower panel of Figure 11, if 125 waves were considered, an underestimation of the liquefaction depth equal to about 18 cm would have been achieved. With the aim to strike the right balance between the accuracy of the results and the involved computational time, by observing both the panels, it appears that 375 random waves should be reproduced at least. If 375 random waves were considered, the computational time would have been saved and an underestimation of only 2% (upper panel) and 3.3% (lower panel) would have been achieved, for the submerged berms characterized by $h_b/h_t = 0.19$ and $h_b/h_t = 0.59$, respectively.

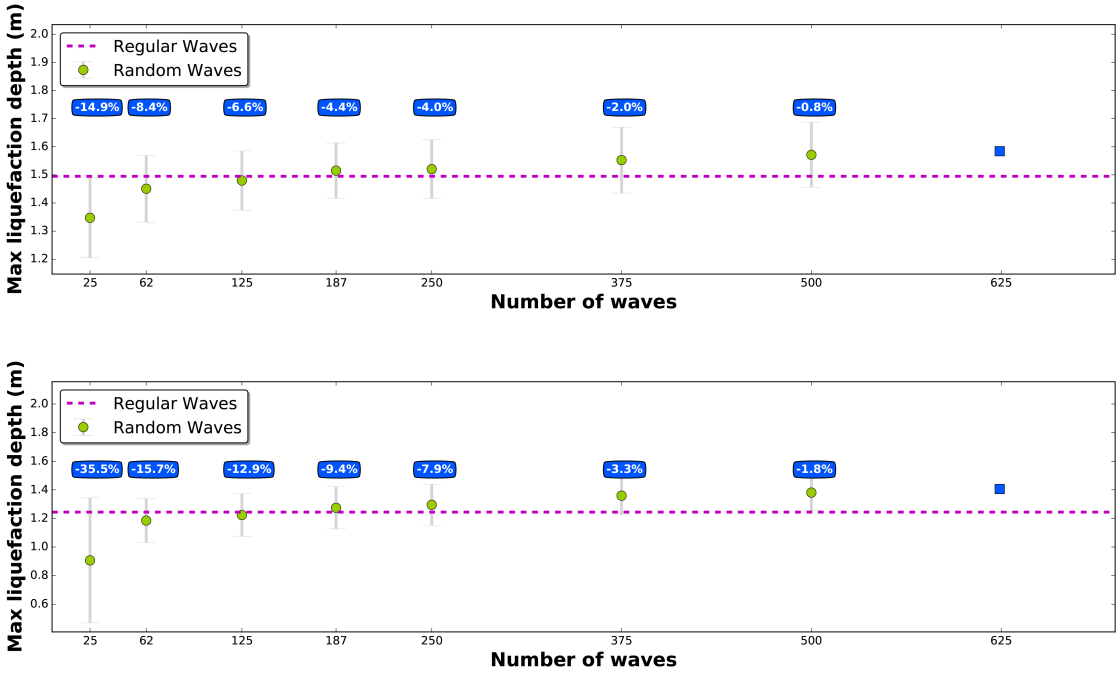

Figure 11. Maximum liquefaction depths as a function of the number of waves. The upper panel refers to submerged berm characterized by $h_b/h_t = 0.19$, $L_b/L_w = 0.35$. The lower panel refers to a submerged berm characterized by $h_b/h_t = 0.59$, $L_b/L_w = 0.35$. The circles refer to the mean values, and vertical lines depict standard deviations.

5. Conclusions

In the present study, the effects of random waves on the momentary liquefaction around a breakwater without and with submerged berms have been investigated. The same numerical tools as in Celli et al. [13] have been applied in the present work. For three different breakwater configurations, the liquefaction depths have been compared with those under the representative regular waves, evaluated by Celli et al. [13]. The adopted soil permeabilities (i.e., k_x = 0.005 m/s and k_z = 0.001 m/s) have made the obtained results valid for medium/coarse sand seabed, characterized by a degree of saturation S_r = 0.975. It should be stressed that this study aims to address the role of randomness of incident waves upon the momentary liquefaction phenomenon by comparing to the numerical results obtained for regular waves [13]. Based on the present study, the main conclusions can be summarized as follows:

(1) Random waves represent more severe loading conditions, resulting in greater liquefaction depths if compared to representative regular waves, characterized by $H = H_{m0}$, $T = T_p$. A safe design should hence be based on the estimation of momentary liquefaction induced by random waves.
(2) The presence of the berm tends to attenuate the random wave-induced momentary liquefaction occurrences in comparison with a conventional breakwater without a berm.
(3) It is confirmed that the largest momentary liquefaction reduction is provided by the berms with the ratio $h_b/h_t = 0.59$, compared to the other two tested configurations. This berm configuration provides a proper pore pressure gradient mitigation and, at the same time, a small reduction of σ_z' in the unloaded areas.
(4) The maximum liquefaction depth estimation requires a minimum of 375 individual waves to be simulated, at least within the tested conditions.

Author Contributions: Conceptualization: D.C., Y.L., M.C.O., M.D.R.–Data curation: D.C.; Formal analysis: D.C., Y.L., M.C.O., M.D.R.–Investigation: D.C.–Methodology: D.C., Y.L., M.C.O., M.D.R.–Project administration: M.C.O., M.D.R.–Resources: M.C.O., M.D.R.–Software: D.C., Y.L., M.C.O., M.D.R.–Supervision: M.C.O., M.D.R.; Validation: D.C.–Visualization: D.C–Writing - original draft: D.C.–Writing - review & editing: D.C., Y.L., M.C.O., M.D.R. All authors have read and agreed to the published version of the manuscript.

Funding: This research received no external funding.

Acknowledgments: This study was partially supported with computational resources provided by the Norwegian Metacenter for Computational Science (NOTUR), under the project No: NN9372K.

Conflicts of Interest: The authors declare no conflict of interest.

References

1. Lamberti, A.; Archetti, R.; Kramer, M.; Paphitis, D.; Mosso, C.; Di Risio, M. European experience of low crested structures for coastal management. *Coast. Eng.* **2005**, *52*, 841–866. [CrossRef]
2. Di Risio, M.; Lisi, I.; Beltrami, G.; De Girolamo, P. Physical modeling of the cross-shore short-term evolution of protected and unprotected beach nourishments. *Ocean. Eng.* **2010**, *37*, 777–789. [CrossRef]
3. Saponieri, A.; Di Risio, M.; Pasquali, D.; Valentini, N.; Aristodemo, F.; Tripepi, G.; Celli, D.; Streicher, M.; Damiani, L. Beach profile evolution in front of storm seawalls: A physical and numerical study. *Coast. Eng. Proc.* **2018**, *1*, 70. [CrossRef]
4. De Girolamo, P.; Di Risio, M.; Beltrami, G.; Bellotti, G.; Pasquali, D. The use of wave forecasts for maritime activities safety assessment. *Appl. Ocean. Res.* **2017**, *62*, 18–26. [CrossRef]
5. Pasquali, D.; Di Risio, M.; De Girolamo, P. A simplified real time method to forecast semi-enclosed basins storm surge. *Estuar. Coast. Shelf Sci.* **2015**, *165*, 61 –69. [CrossRef]
6. Pasquali, D.; Bruno, M.; Celli, D.; Damiani, L.; Di Risio, M. A simplified hindcast method for the estimation of extreme storm surge events in semi-enclosed basins. *Appl. Ocean. Res.* **2019**, *85*, 45–52. [CrossRef]
7. Van Gent, M.R. Rock stability of rubble mound breakwaters with a berm. *Coast. Eng.* **2013**, *78*, 35–45. [CrossRef]
8. Celli, D.; Pasquali, D.; De Girolamo, P.; Di Risio, M. Effects of submerged berms on the stability of conventional rubble mound breakwaters. *Coast. Eng.* **2018**, *136*, 16–25. [CrossRef]

9. Zen, K.; Yamazaki, H. Mechanism of wave-induced liquefaction and densification in seabed. *Soils Found.* **1990**, *30*, 90–104. [CrossRef]
10. Nago, H.; Maeno, S.; Matsumoto, T.; Hachiman, Y. Liquefaction and densification of loosely deposited sand bed under water pressure variation. In Proceedings of the Third International Offshore and Polar Engineering Conference, Singapore, 6–11 June 1993; International Society of Offshore and Polar Engineers: Mountain View, CA, USA, 1993.
11. Sassa, S.; Sekiguchi, H. Wave-induced liquefaction of beds of sand in a centrifuge. *Geotechnique* **1999**, *49*, 621–638. [CrossRef]
12. Sumer, B.M. *Liquefaction around Marine Structures*; World Scientific: Singapore, 2014.
13. Celli, D.; Li, Y.; Ong, M.; Di Risio, M. The role of submerged berms on the momentary liquefaction around conventional rubble mound breakwaters. *Appl. Ocean. Res.* **2019**, *85*, 1–11. [CrossRef]
14. Sumer, B.M.; Fredsøe, J.; Christensen, S.; Lind, M. Sinking/floatation of pipelines and other objects in liquefied soil under waves. *Coast. Eng.* **1999**, *38*, 53–90. [CrossRef]
15. Liu, H.; Jeng, D.S. A semi-analytical solution for random wave-induced soil response and seabed liquefaction in marine sediments. *Ocean Eng.* **2007**, *34*, 1211–1224. [CrossRef]
16. Xu, H.; Dong, P. A probabilistic analysis of random wave-induced liquefaction. *Ocean Eng.* **2011**, *38*, 860–867. [CrossRef]
17. Zhao, H.; Jeng, D.S.; Zhang, J.; Liao, C.; Zhang, H.; Zhu, J. Numerical study on loosely deposited foundation behavior around a composite breakwater subject to ocean wave impact. *Eng. Geol.* **2017**, *227*, 121–138. [CrossRef]
18. Kudella, M.; Oumeraci, H.; de Groot, M.B.; Meijers, P. Large-Scale Experiments on Pore Pressure Generation underneath a Caisson Breakwater. *J. Waterw. Port Coast. Ocean Eng.* **2006**, *132*, 310–324. [CrossRef]
19. Ye, J.; Jeng, D.; Wang, R.; Zhu, C. Numerical simulation of the wave-induced dynamic response of poro-elastoplastic seabed foundations and a composite breakwater. *Appl. Math. Model.* **2015**, *39*, 322–347. [CrossRef]
20. Zijlema, M.; Stelling, G.; Smit, P. SWASH: An operational public domain code for simulating wave fields and rapidly varied flows in coastal waters. *Coast. Eng.* **2011**, *58*, 992–1012. [CrossRef]
21. Li, Y.; Ong, M.C.; Tang, T. Numerical analysis of wave-induced poro-elastic seabed response around a hexagonal gravity-based offshore foundation. *Coast. Eng.* **2018**, *136*, 81–95. [CrossRef]
22. Zijlema, M.; Stelling, G.S. Further experiences with computing non-hydrostatic free-surface flows involving water waves. *Int. J. Numer. Methods Fluids* **2005**, *48*, 169–197. [CrossRef]
23. Zijlema, M.; Stelling, G. Efficient computation of surf zone waves using the nonlinear shallow water equations with non-hydrostatic pressure. *Coast. Eng.* **2008**, *55*, 780–790. [CrossRef]
24. Smit, P.; Zijlema, M.; Stelling, G. Depth-induced wave breaking in a non-hydrostatic, near-shore wave model. *Coast. Eng.* **2013**, *76*, 1–16. [CrossRef]
25. Biot, M.A. General theory of three-dimensional consolidation. *J. Appl. Phys.* **1941**, *12*, 155–164. [CrossRef]
26. Li, Y.; Ong, M.C.; Tang, T. A numerical toolbox for wave-induced seabed response analysis around marine structures in the OpenFOAM® framework. *Ocean Eng.* **2020**, *195*, 106678. [CrossRef]
27. Celli, D.; Pasquali, D.; Di Nucci, C.; Di Risio, M. The Effects of Submerged Berms on the Seabed Pressure around Rubble Mound Breakwaters. In Proceedings of the Coastal Structures Conference 2019, Hannover, Germany, 29 September–2 October 2019; pp. 306–313.
28. Suzuki, T.; Altomare, C.; Veale, W.; Verwaest, T.; Trouw, K.; Troch, P.; Zijlema, M. Efficient and robust wave overtopping estimation for impermeable coastal structures in shallow foreshores using SWASH. *Coast. Eng.* **2017**, *122*, 108–123. [CrossRef]
29. Valentini, N.; Damiani, L.; Molfetta, M.G.; Saponieri, A. New coastal video-monitoring system achievement and development. *Coast. Eng. Proceedings* **2017**, *1*, 11. [CrossRef]
30. Valentini, N.; Saponieri, A.; Danisi, A.; Pratola, L.; Damiani, L. Exploiting remote imagery in an embayed sandy beach for the validation of a runup model framework. *Estuar. Coast. Shelf Sci.* **2019**, *225*, 106244. [CrossRef]
31. Van den Bos, J.; Verhagen, H.J.; Zijlema, M.; Mellink, B. Towards a practical application of numerical models to predict wave-structure interaction: An initial validation. *Coast. Eng. Proceedings* **2014**, *1*, 50. [CrossRef]

32. Van den Bos, J.; Verhagen, H.J.; Kuiper, C. Numerical modelling of wave reflection and transmission in vertical porous structures. In Proceedings of the 7th Coastal Structures conference (ASCE-COPRI), Boston, MA, USA, 9–11 September 2015.
33. Tsai, C.P.; Lee, T.L. Standing wave induced pore pressures in a porous seabed. *Ocean Eng.* **1995**, *22*, 505–517. [CrossRef]
34. Bierawski, L.; Maeno, S. Water pressure fluctuation around a submerged breakwater. In *Proceedings of the Symposium on Dynamic Water Pressure and Bed Response in the Water*; DPRI, Kyoto University: Kyoto, Japan, 2002.
35. Sakai, T.; Hatanaka, K.; Mase, H. Wave-induced effective stress in seabed and its momentary liquefaction. *J. Waterw. Port Coast. Ocean. Eng.* **1992**, *118*, 202–206. [CrossRef]
36. Liu, H.; Jeng, D.S. Response of a porous seabed under random wave loading. In Proceedings of the 25th International Conference on Offshore Mechanics and Arctic Engineering, Hamburg, Germany, 4–9 June 2006; American Society of Mechanical Engineers: New York, NY, USA, 2006; pp. 85–93.
37. Goda, Y. *Random Seas and Design of Maritime Structures*; World Scientific: Singapore, 2010.
38. Jeng, D.S.; Ye, J.H.; Zhang, J.S.; Liu, P.F. An integrated model for the wave-induced seabed response around marine structures: Model verifications and applications. *Coast. Eng.* **2013**, *72*, 1–19. [CrossRef]
39. Sui, T.; Zheng, J.; Zhang, C.; Jeng, D.S.; Zhang, J.; Guo, Y.; He, R. Consolidation of unsaturated seabed around an inserted pile foundation and its effects on the wave-induced momentary liquefaction. *Ocean Eng.* **2017**, *131*, 308–321. [CrossRef]